MATERIALS SCIENCE

Molecular insights on the crystalline cellulose-water interfaces via three-dimensional atomic force microscopy

Ayhan Yurtsever[1]*, Pei-Xi Wang[2]†, Fabio Priante[3], Ygor Morais Jaques[3], Keisuke Miyazawa[1], Mark J. MacLachlan[1,2], Adam S. Foster[1,3], Takeshi Fukuma[1]*

Cellulose, a renewable structural biopolymer, is ubiquitous in nature and is the basic reinforcement component of the natural hierarchical structures of living plants, bacteria, and tunicates. However, a detailed picture of the crystalline cellulose surface at the molecular level is still unavailable. Here, using atomic force microscopy (AFM) and molecular dynamics (MD) simulations, we revealed the molecular details of the cellulose chain arrangements on the surfaces of individual cellulose nanocrystals (CNCs) in water. Furthermore, we visualized the three-dimensional (3D) local arrangement of water molecules near the CNC surface using 3D AFM. AFM experiments and MD simulations showed anisotropic water structuring, as determined by the surface topologies and exposed chemical moieties. These findings provide important insights into our understanding of the interfacial interactions between CNCs and water at the molecular level. This may allow the establishment of the structure-property relationship of CNCs extracted from various biomass sources.

INTRODUCTION

Cellulose is an abundant and renewable resource produced by plants as well as some bacteria, fungi, and tunicates (*1*). Its low toxicity, biodegradability, excellent mechanical properties, and adaptable surface chemistry make it attractive for producing diverse functional nanomaterials (*2*–*5*). In the 1940s, Rånby (*6*, *7*) demonstrated that the treatment of biomass with sulfuric acid can yield nanocrystals of cellulose, now called cellulose nanocrystals (CNCs). CNCs are three-dimensional (3D) crystalline assemblages of individual cellulose chains, formed through inter- and intramolecular hydrogen bonds (HBs; Fig. 1, A and B). Notably, the size, crystal structure, degree of crystallinity, and surface chemistry of CNCs depend on the biomass source (such as cotton or wood), digestion conditions, and acid used in the hydrolysis (*8*). Typically, CNCs are 2 to 30 nm in diameter and several hundred nanometers long (*1*). The work of Rånby went mostly unnoticed, but the field was revived in 1992 when Gray and colleagues (*9*) found that CNCs form a chiral nematic liquid-crystalline order in water. Over the past 25 years, the field of CNCs has exploded (*5*, *10*), and these fascinating rod-shaped nanomaterials have been explored for a wide variety of applications, including rheology modifiers (*11*), composite structures (*12*), drug delivery (*13*), cell scaffolds (*14*), flexible organic electronics (*15*), tissue engineering (*16*), and photonic materials (*17*), and as templates for fabricating iridescent glass and other materials with chiral structures (*18*).

Although the bulk properties of CNCs, including surface charge, dimensions, chemical composition, thermal stability, and crystallinity, are easily measured (*1*), a detailed understanding of the surface chemistry and structure of individual CNC particles is yet to be achieved. The properties of cellulose-derived nanomaterials strongly depend on the structural details of the exposed crystal planes. The crystalline order and structure at the interface influence the interfacial interactions between CNCs and other cellulosic nanomaterials and affect the structure and percolating properties of the CNC-matrix interface (*19*). Furthermore, chemistry involving cellulose takes place in aqueous environments. Therefore, gaining an understanding of the interfacial interactions of CNCs with other nanomaterials such as other polysaccharides, polymer matrices, and biomolecules requires probing the spatial distribution of 3D local hydration structures near the cellulose-water interface (*20*). Although cellulose-water interactions are important and have been extensively studied (*21*–*24*), no experimental studies have explored the molecular-level 3D organization of hydration structures near the cellulose surface. The structuring of water molecules at the interface is an essential factor in determining the performance of composite nanomaterials and the conversion efficiency of cellulose biomass into renewable energy (*10*, *25*, *26*). The structural properties of interfacial water structuring are considered effective in mediating the cholesteric ordering of self-assembled CNCs (*20*). The molecular-level characterization of the 3D local hydration structures at cellulose-water interfaces would thus contribute to a better understanding of the liquid-crystalline self-assembly of CNCs, which is of fundamental importance and can provide a new route for creating functional nanomaterials with tunable optical and mechanical properties (*27*).

Transmission electron microscopy (TEM) studies have revealed a twisted structure of CNCs (*28*, *29*), and under certain conditions, they have provided cross-sectional shapes and the corresponding lattice images of ultrathin sections of *Valonia* and tunicate microfibrils (*30*–*32*). However, cross-sectional shapes of plant-based CNCs are not yet available. On the other hand, atomic force microscopy (AFM) has been used to image the size and shapes of CNCs in many studies (*33*), providing data that corroborate the electron microscopy data. Various groups have investigated the elastic properties of

[1]Nano Life Science Institute (WPI-NanoLSI), Kanazawa University, Kakuma-machi, Kanazawa 920-1192, Japan. [2]Department of Chemistry, University of British Columbia, 2036 Main Mall, Vancouver, BC V6T 1Z1, Canada. [3]Department of Applied Physics, Aalto University, Helsinki FI-00076, Finland.
*Corresponding author. Email: yurtsever@staff.kanazawa-u.ac.jp (A.Y.); fukuma@staff.kanazawa-u.ac.jp (T.F.)
†Present address: i-Lab, Suzhou Institute of Nano-Tech and Nano-Bionics (SINANO), Chinese Academy of Sciences, 398 Ruoshui Road, Dushu Lake Higher Education Town, Suzhou, Jiangsu 215123, P. R. China.

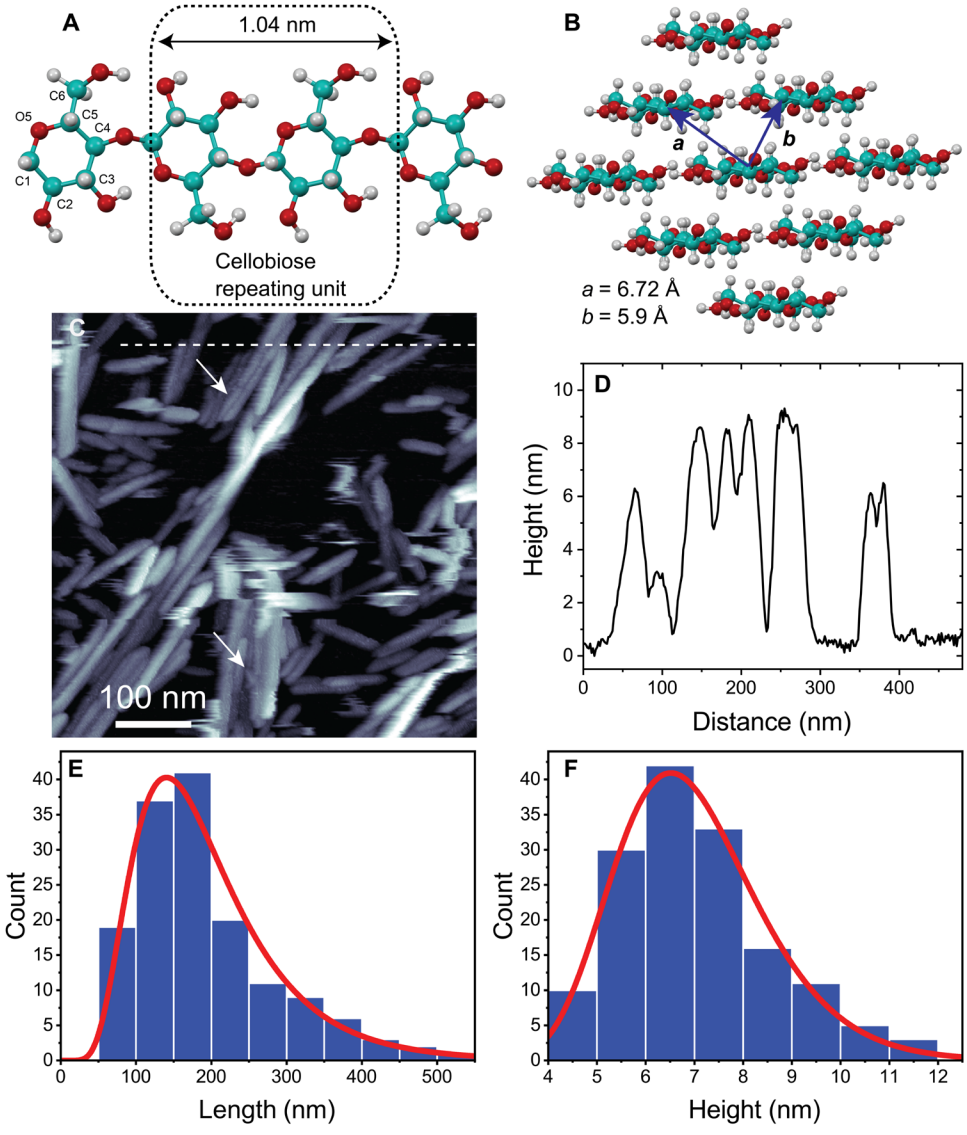

Fig. 1. Structural overview of a CNC. (**A**) Chemical structure of cellulose and the repeating unit cellobiose are illustrated. (**B**) Representation of unit cell of cellulose I_α structure. Carbon, oxygen, and hydrogen atoms are represented by cyan, red, and white colors, respectively. (**C**) AFM topography image showing the quasi-rod–shaped nanostructure of CNCs immobilized on an APTES-modified mica substrate with lengths in the range of 75 to 500 nm. In addition to individual CNCs, some laterally associated CNC particles represented by white arrows can also be seen. (**D**) A representative line profile (averaged) taken along the white dashed line shown in (C). (**E**) Length distribution histogram of CNC with a lognormal fit. (**F**) Height distribution histogram of CNC with a lognormal fit.

wood- and tunicate-derived CNCs (*34*, *35*). The chiral characteristics of various CNCs with different dimensions and compositions have been studied using AFM (*28*, *36*). Real-time visualization of single-molecule adsorption dynamics, activities of individual proteins, and degradation of crystalline cellulose by cellulase enzymes have been imaged using AFM (*37*, *38*). In the late 1990s, Baker, Miles, and co-workers (*39*–*41*) applied high-resolution AFM to the surface of microcrystalline cellulose extracted from *Valonia ventricosa*, a green alga known to have highly crystalline cellulose. They successfully identified the cellulose structure on the surface of the fibers and correlated it with the known structures of cellulose I_α. Hanley *et al.* (*36*) obtained TEM and AFM images of *Micrasterias denticulata* cellulose microfibrils. These studies have substantially contributed to our understanding of the crystalline structure of native cellulose. To date, atomic/molecular-resolution images of plant-based CNCs have not been reported, although they will be of great interest to researchers investigating CNCs. The smaller size, lower crystallinity, and inhomogeneous nature of CNCs compared to the microfibers of *Valonia*, having large cross-sectional dimensions and a high degree of crystallinity and purity, present a considerable challenge for detailed AFM studies.

Here, we provide molecular-scale structural details of cellulose chain arrangements on the surfaces of individual CNCs derived from coconut gels (bacterial cellulose, also known as nata-de-coco), using AFM in water. Molecularly resolved AFM images acquired on an individual CNC-water interface revealed periodicities along the cellulose chain axis, corresponding to the cellobiose repetition and glucose interval. High-resolution AFM images revealed the

presence of domains with triclinic organization of molecular chains, corroborating the triclinic I_α crystalline structure of the surface. Moreover, the organization of water molecules near different crystalline facets of CNCs was characterized using 3D AFM combined with molecular dynamics (MD) simulations. We found that the laterally structured water layers followed the rugged contours of the underlying cellulose surface, displaying a distinct hydration pattern due to the specific arrangement of surface functional groups. The observed anisotropy and differences between the different crystalline interfaces reflect the dual hydrophilic and lipophilic behavior of CNCs and affect their mechanical, intermolecular, and interfacial properties. These studies elucidate the supramolecular structure of the CNCs, and the disorder present in individual fibers, and provide a better understanding of the interfacial interactions between CNCs and water at the molecular level. The specific solvation structures formed at the interfaces may influence the reactivity in the chemical and enzymatic hydrolysis of lignocellulosic biomass and other natural polysaccharides and contribute to the slowing of the reaction rate in cellulose conversion processes over time, as has been experimentally observed (*42*). Overall, these findings will be valuable for researchers in diverse fields, such as soft matter physics and sustainable biomaterials, as well as for fundamental science in understanding water structuring on biopolymer surfaces with hydrophobic and hydrophilic domains, such as protein- and peptide-based structural biopolymers.

RESULTS

Structural characterization of CNCs

A typical AFM image of CNCs immobilized on a 3-aminopropyltriethoxysilane (APTES)–modified mica substrate, acquired in water, is shown in Fig. 1C. The AFM images collected from various samples confirmed that the pristine CNCs displayed a quasi-rod–like morphology with ~20-nm width and 75- to 500-nm length (as seen from the representative line profile in Fig. 1D), which agrees with the average CNC diameter determined previously from TEM and AFM measurements (*43*). However, owing to the well-known tip-broadening effects, the apparent width of the CNCs was relatively larger than the actual value. The width of the CNCs was determined from their height measurements, to avoid tip-broadening effects on the width measurements. The AFM height and length distribution histograms of the CNC fibers with lognormal fits are shown in Fig. 1 (E and F). The average height of the CNC fibers on APTES-modified mica substrate was found to be ~7.0 ± 1.5 nm, which is in line with the previous AFM studies (*44*, *45*), after incorporating the tip-broadening effects. The length of the CNCs was found to be 75 to 500 nm with a mean value of 196.8 nm. In addition to the isolated CNC fibers, small agglomerates arranged in a side-by-side fashion were also observed (some of them are marked by white arrows), similar to the results obtained in several other studies (*33*). The formation of these CNC aggregates and bundles has been explained by the reduction in the charge density of CNC particles during the acid hydrolysis process (*28*, *46*). The colloidal stability of the CNCs was mainly provided by the negatively charged sulfate groups introduced on the crystal surface, which resulted from the substitution of some of the surface hydroxyl groups by sulfate ions. The reduced charges on the CNC surfaces due to the incomplete hydrolysis process make them prone to flocculation. Contrary to the model structures with sharp edges, and square or hexagonal profiles, the individual CNC fibers exhibit a smooth and round cross-sectional shape owing to the tip convolution effect (Fig. 1C and figs. S1 to S4).

The structural defects present on some CNC surfaces were also identified as breaks in the continuity of the cellulose chains in certain regions with irregular intervals along the axis of the CNC fiber (Fig. 2). The white arrows in Fig. 2A indicate the areas where some darker patches ~8 to 10 nm wide running across the CNC fibers can be seen (Fig. 2B). These darker regions (apparently 1 nm deep) between the bright domains are attributed to the presence of structural defects existing in the low-ordered amorphous domains of the CNCs because of the inadequate hydrolysis process, or probably due to imperfect association of protofibrils to form microfibrils. Although the acid hydrolysis of cellulosic feedstocks was expected to obliterate the amorphous region or noncellulosic contents of the CNC particles (*1*, *8*), leaving only the crystalline part, this result indicates that the noncrystalline phase is still present in some CNC particles. However, the possibility of the degradation of CNCs by water could not be excluded. The existence of a different type of defect is demonstrated in Fig. 2C, where, in addition to a well-ordered periodic structure (red arrows), a disordered domain with bright diffusive protruding features (apparently 0.5 nm high) appears on the CNC surface (Fig. 2D). These features are thought to be due to unstable hydration structures or hydrolyzed surface products (see discussion below). While the x-ray and neutron diffraction techniques provide valuable structural information about the crystalline regions, they often provide less information about the amorphous domains.

High-resolution imaging of the ordered (crystalline) and disordered (amorphous) regions in the same CNC fiber was successfully performed. A high-resolution image of the ordered domain is shown in Fig. 2E. In addition to resolving the individual cellulose chains, a series of periodic features aligned perpendicular to the long crystallographic molecular axis can be observed on individual CNCs (red arrows in Fig. 2, F and G). An interval of 1.05 nm was determined from the 2D–fast Fourier transform (FFT) spectra and the line profile analysis (Fig. 2H), which is similar to that previously observed for highly crystalline *Valonia* celluloses with large cross-sectional profiles (*39*, *40*, *45*). On the basis of the comparison of the Connolly surfaces of the different crystalline planes, the observed surface features along the chain axis were previously attributed to the topographic difference between the hydroxymethyl groups exposed on the O5-C5 face of the glucose ring (Fig. 1A) due to the twofold screw symmetry of the cellulose chain. Nevertheless, it is important to note that AFM images obtained in liquids are a convolution of the surface topographic features and hydration layers (*47*). As detailed in the next section, we found that the underlying cellulose crystalline planes template the lateral molecular arrangement of the interfacial water molecules according to their molecular structures. Thus, the interfacial water structures represent the symmetry of the underlying cellulose nanostructures. We found that the cellobiose repeat interval was more likely to be resolved in high-resolution AFM images along the chain direction, which is in line with a previous study (*40*). Further examples from different samples are presented in figs. S4 (D and F) and S5B, which exemplify the cases in which both the cellobiose and glucose repeating units were resolved along the chain direction.

AFM images collected on various CNC surfaces exhibited distinct surface morphologies. On some CNC surfaces, the molecular chains were observed to be well ordered and stable, whereas the other sites were observed to fluctuate, showing no features. In some cases, the

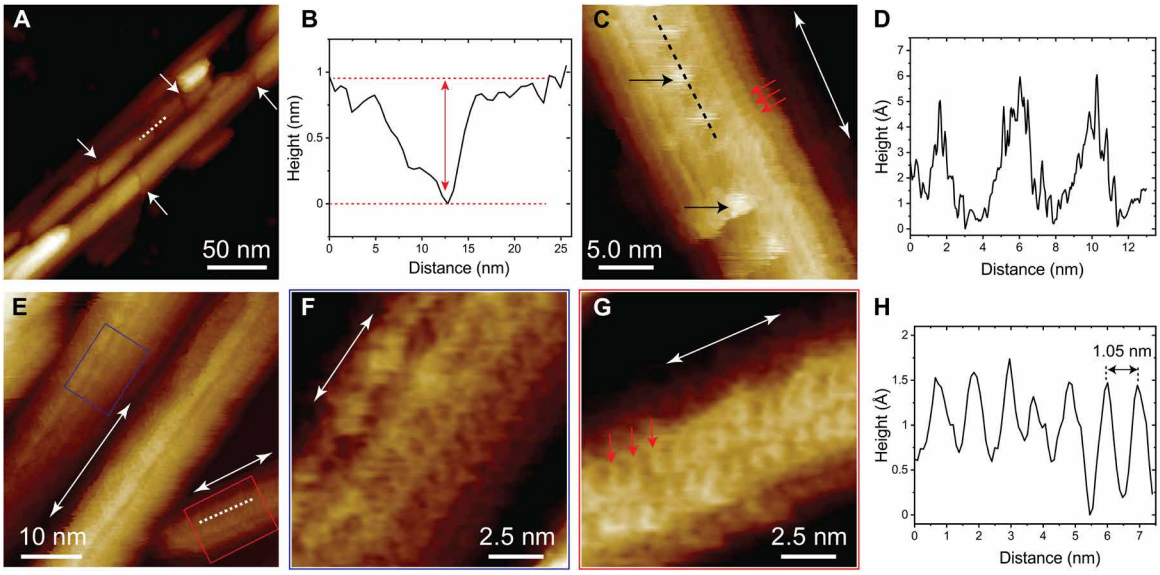

Fig. 2. Observation of structural defects. (**A**) AFM image of CNCs showing the presence of vertically aligned dark patches (indicated by white arrows) distributed at irregular intervals along the length of a CNC fiber. The dark region between the bright domains represents the structural defects that remained after acid hydrolysis treatment. (**B**) Representative line profile plotted along the white dashed line shown in (A), indicating a depression of approximately 1 nm over the amorphous domain with approximately 10-nm width. (**C**) High-resolution AFM image showing a different type of surface defect with bright diffusive appearance (marked by black arrows). (**D**) Line profile plotted along the black dashed line shown in (C). (**E**) High-resolution AFM image acquired over the crystalline domains, showing the well-ordered cellulose chain arrangements at the surface. (**F** and **G**) Enlarged images of the blue- and red-framed regions shown in (E), respectively. (**H**) Line profile taken along the cellulose chain axis [white dashed line in (E)] further confirms the presence of an interval of 1.05 nm, corresponding to the cellobiose repeat unit. The arrowhead represents the direction of cellulose molecular chains on the image.

chains appeared to be less ordered (fig. S1). There are several possible explanations for this observation. The molecular mobility on the CNC surface in contact with water and the changes in the surface hydroxymethyl, sulfate, and OH group conformations induced by the interaction with water molecules might have led to the observed differences in the surface morphology. Previous evidence indicated that the surface chains of hydrated CNC particles are more mobile than the interior chains (*48*, *49*). MD simulations and solid-state nuclear magnetic resonance measurements have demonstrated that the presence of water interactions with the CNC surfaces induces additional disorder in the surface glucose chains, and this disorder expands toward the core of the cellulose fiber (*50*). The existence of different crystallographic planes and crystalline phases (i.e., I_α versus I_β), which might have different interaction affinities with water, might also be the reason for the observed differences in the morphology of CNC particles in the high-resolution images. The different characteristics of the interactions at the interface may only result in stable hydration layer structures in specific domains. Cellulose microfibrils have different hydrophobic and hydrophilic surfaces with distinct abilities to form HBs (*1*, *51*). Moreover, the relative strength of the interaction between water and the different surface structures can lead to regions of apparent instability, resulting in the appearance of fluctuating features in some AFM images (Fig. 2C and figs. S1 and S2).

Our results indicate that the size of the crystalline domains perpendicular to the chain direction was relatively small compared to those in the axial chain direction. The absence of long-range crystallographic ordering in the lateral direction, also observed in other studies, confirms that cellulose chains on the outer surface are generally less ordered than those in the interior region (*45*, *52*). The dynamic changes occurring at the CNC surfaces in contact with water, combined with the poor crystallographic ordering in the direction perpendicular to the chain axis, make it challenging to obtain high-resolution structural details over a large surface area.

To further examine the structural details of the CNC-water interfaces, we performed localized AFM observations on an individual CNC surface. A representative AFM topography image of a part of an individual CNC fiber with large crystalline domains is presented in Fig. 3A, revealing the coexistence of two different molecular arrangements at the crystal-water interfaces. This implies that the native cellulose NCs exhibit heterogeneous crystalline structures. The molecularly resolved AFM image (on the left side of the surface) revealed the details of the molecular organization at the interface, showing honeycomb or zigzag chain arrangements, along with the protruding structural features between the zigzag patterns (marked with the white dashed circle and oval in Fig. 3B). The line profile along the white dashed line in Fig. 3B is shown in Fig. 3C. The FFT pattern obtained from the image data in Fig. 3B is shown in Fig. 3D, providing the periodicities of prominent surface features. Two spacings can be identified from the FFT spectra and line profile analysis along the chain axis (Fig. 3, C and D), the 0.54- and 1.09-nm periodicities, closely matching the glucose interval (0.52 nm) and cellobiose repeat distance (1.04 nm), respectively.

A close inspection of the AFM images in Fig. 3 (A, B, and E) further indicates that the neighboring cellulose chains are displaced only in one direction. There is also a pattern of bright protruding molecular features (marked with white dashed circles) aligned diagonally to the cellulose molecular axis at an angle of 67°, suggesting that the cellulose I_α phase was resolved at the interface. It has been well established that naturally occurring cellulose can exist in two distinct crystalline allomorphs: the one-chain triclinic I_α and the

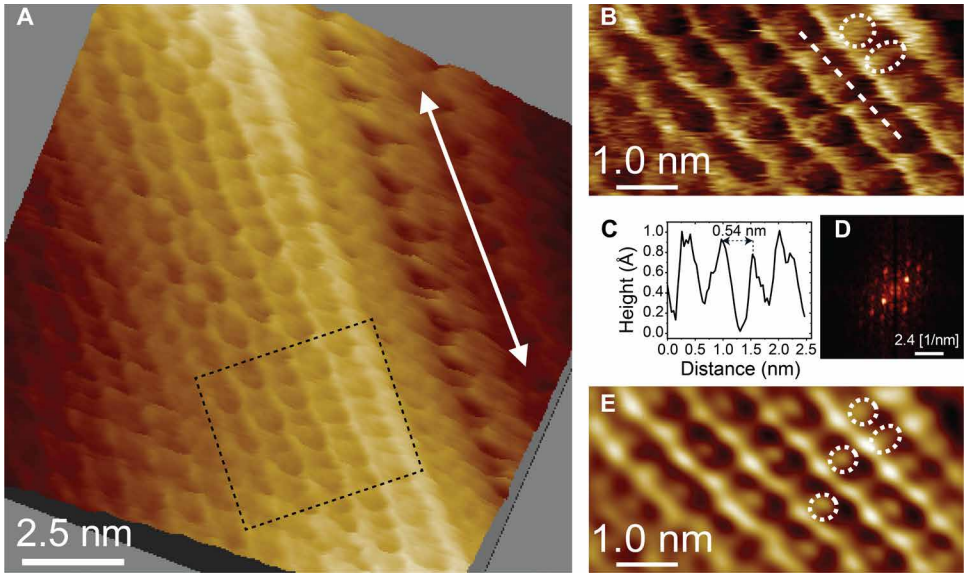

Fig. 3. Molecular-resolution image of the CNC-water interface. (**A**) High-resolution AFM topography image of an individual CNC surface, revealing the details of the molecular organization at the interface. The different arrangements of chains over the surface can be seen. The arrowhead represents the direction of cellulose molecular chains. (**B**) Enlarged AFM image of the region highlighted in a black dashed frame in (A), showing the honeycomb arrangement of cellulose chains at the interface. (**C**) A representative line profile (averaged) taken along the white dashed line marked in (B). (**D**) The 2D-FFT pattern taken from the image data in (B) highlights the prominent surface periodicities. (**E**) The reconstructed image of the surface in (B), obtained by executing inverse 2D-FFT spectra. Zigzag molecular arrangements of cellulose chains can be seen.

two-chain monoclinic I_β (*53*). The relative proportions of these two distinct crystalline structures (i.e., I_α/I_β) vary with biomass source (*53*). Although there is limited consensus on the I_α/I_β ratio, the celluloses obtained from algae and bacteria are generally rich in the I_α phase (*54*, *55*), whereas those obtained from the higher woody plants generally contain a high fraction of the I_β phase (*56*). These two crystalline forms differ in their hydrogen-bonding patterns, but both have the same repeat distance. In the case of the I_β phase, the neighboring sheets of cellulose were displaced alternately from each other by a quarter of the unit cell in the *c* direction. This differs from the I_α phase, where the neighboring chains are displaced regularly in one direction, exhibiting a diagonally shifted pattern in the high-resolution AFM images (Fig. 3 and fig. S6A). This is in agreement with the fact that CNCs derived from coconut gels exhibit bacterial cellulose characteristics. They are slightly different from plant-derived CNCs.

3D-AFM characterization of hydration structures at CNC-water interfaces

We performed 3D-AFM force measurements on a selected CNC surface with typical dimensions of 12 nm by 12 nm by 3 nm (128 × 128 × 256 pixels) to characterize the local 3D water-molecular arrangements at the cellulose-water interfaces in more detail (see Materials and Methods for further details). 3D AFM has been previously applied to characterize the interfacial solvation structures and properties of various surfaces/interfaces with submolecular spatial resolution, including the spatial distribution of ions (*57*–*62*). However, in the past, 3D-AFM measurements were performed mainly on stable and atomically flat surfaces. The molecular-level characterization of hydration structures above the curved surfaces with irregular shapes and heterogeneous chemistries is challenging because the observed particles are often displaced on the surface during 3D-AFM force measurements using a relatively stiff AFM cantilever, which is required to penetrate the hydration shells and characterize their molecular structures.

A schematic drawing in Fig. 4A illustrates the 3D-AFM force mapping experiment on a solid substrate and a description of the 2D *xz* and *xy* planes in the 3D map. A typical 3D-AFM image of the cellulose-water interface is presented in Fig. 4 (B and C), showing the variations in Δf of an oscillating AFM cantilever in the 3D interfacial space. The resulting 3D map shows a well-ordered water structure in the vicinity and across the entire *xy* crystalline plane of the CNC surfaces. The overlaid vertical 2D Δf maps represent structurally ordered water layers along both perpendicular and parallel directions to the cellulose molecular axis. The horizontal 2D Δf maps reconstructed from the 3D map at the vertical positions marked with black, blue, and red arrows in Fig. 4G are presented in Fig. 4 (D to F), respectively. These 2D Δf slices reflect the in-plane organization of structured water molecules in the hydration layers near the cellulose surface. A contrast inversion of the hydration pattern occurred, moving from a closer to a relatively further distance from the cellulose surface. The hydration structure with bright, extended, and protruding molecular features changed into a pattern with dark-contrast depression. A honeycomb arrangement of interfacial water molecules was evident in the upper-right part of the image (Fig. 4F).

The vertical 2D Δf slices obtained through the AB-*z*, CD-*z*, and EF-*z* planes for different lateral trajectories are displayed in Fig. 4 (G to I). The vertical 2D Δf maps show undulating hydration profiles with bright and extended hydration features closer to the cellulose surface (marked with blue dashed ellipses), followed by a pattern of empty gaps (white dashed ellipses). The periodicity of the molecular features (marked with dashed blue ellipses in Fig. 4G) aligned along the chain axis was approximately 1.08 nm, closely matching the fiber repeat distance of 1.04 nm.

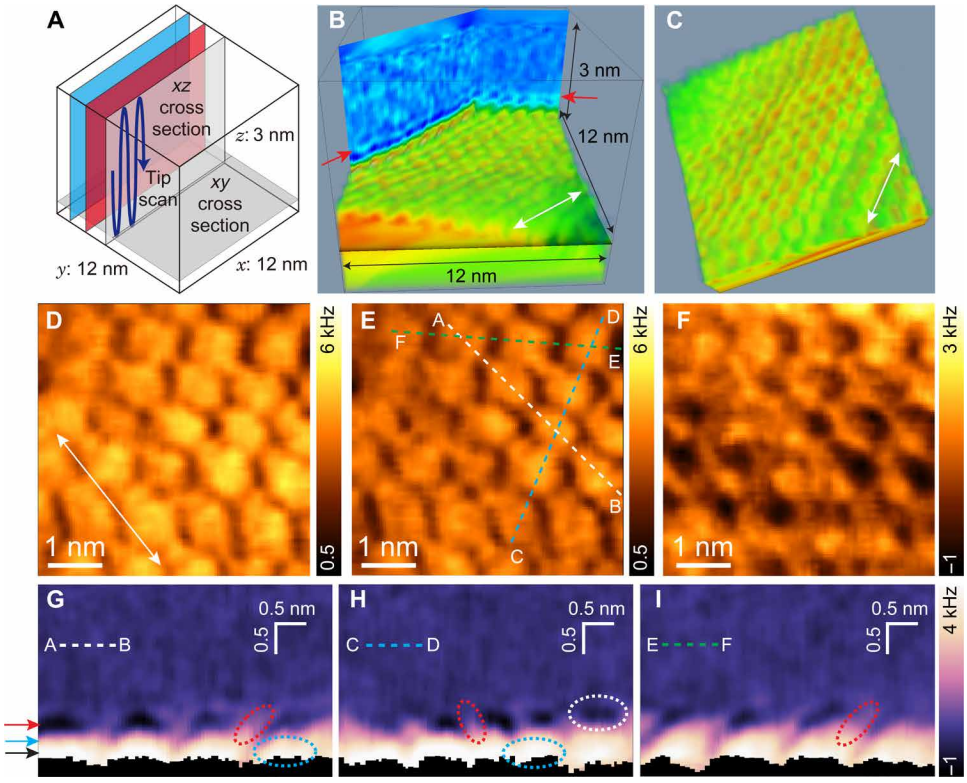

Fig. 4. A representative 3D-AFM image of the cellulose-water interface. (**A**) Illustration of 3D-AFM principle and a description of the 2D *xz* and *xy* slices in the 3D map. (**B**) 3D-AFM image of the cellulose-water interface acquired over the CNC surface shown in Fig. 3A. The 3D map indicates the variations of Δf of the oscillating cantilever in the 3D interfacial space. The red arrows indicate the ordered layer of water molecules at the interface. (**C**) Top view of the interface. (**D** to **F**) Horizontal 2D *xy* Δf maps of the cellulose-water interface extracted from the 3D volume map at the vertical *z* positions marked by black, blue, and red arrows in (G). A pronounced ordering of water molecules can be seen here. (**G** to **I**) Vertical 2D *xz* Δf maps of the cellulose-water interface taken along the dashed lines marked in (E). The force mapping area has a dimension of 12 nm by 12 nm and is divided into grids of 256 × 256 pixels. The frequency and amplitude of the *z* modulation signal during 3D-AFM force mapping were 195.3 Hz and 3 nm, respectively.

We found that the 3D-AFM maps of cellulose-water interfaces taken from different crystalline surfaces showed inhomogeneous water structuring exhibiting different hydration patterns, distributions, and stabilities. These reflect the dual amphiphilic character of the cellulose surface with varying molecular chain arrangements and packing with different hydrogen-bonding abilities (figs. S3 to S7). In addition to a well-ordered hydration structure (see Figs. 3 and 4 and figs. S3, D and E; S4, E, F, and H; and S7, B and C), a disordered and fluctuating hydration feature was also observed in some regions of the CNC surface (framed areas in figs. S3F and S4G). This might be caused by instabilities in the hydration layer, suggesting that water molecules cannot form strongly localized hydration structures in certain domains or crystalline planes.

We performed MD simulations to provide a molecular-level understanding of the observed organization of water molecules near the different crystalline interfaces of the CNCs (Fig. 5). Various molecular models of the structure of elementary fibrils have been proposed for CNCs from higher plants (*63*, *64*). These include 18-chain, 24-chain, and 36-chain models with hexagonal, diamond, and rectangular cross sections with multiple surfaces. The CNC structures were built with a hexagonal shape, as suggested by Ding and Himmel (*64*), where the (100), (010), and (110) surface facets were exposed as hydrophilic and hydrophobic planes, respectively (*52*). MD simulations were performed on a model of I_α CNCs constructed by hexagonal arrangements of 36 chains organized into eight layers (Fig. 5, A to C). The 3D water-oxygen density distribution around the different crystalline planes of the hexagonal-shaped CNC is shown in Fig. 5D. The resulting MD simulations revealed that the cellulose crystalline planes highly structure the water molecules in their contact, yielding an intricate 3D structural ordering at the interface with water molecules confined with increased density at specific surface regions. The crystalline planes labeled with numbers (1), (2), and (3) exhibited distinctly different water density distributions because of the heterogeneous nature of their surface topology and chemistry, displaying numerous OH groups with different polarities, including exposed CH and OH chemical moieties (Fig. 5, D and E, and figs. S8 to S10). This highly anisotropic water structuring extends by about 0.8 nm from the surface into the bulk water, as can be evidenced by the averaged 1D water-oxygen density profile (Fig. 5F). It should be noted that the solvent density distributions of the diametrically opposed planes of the crystal mirror each other, showing identical molecular patterns.

To provide further insight into the water structuring at each of these interfaces, we calculated planar 2D water-oxygen density distributions, as shown in Fig. 5 (G to I). The white and red arrows in Fig. 5E indicate the vertical positions where the horizontal 2D *xy* density maps were extracted from the 3D density distribution data. The water-oxygen density distributions above the crystalline plane

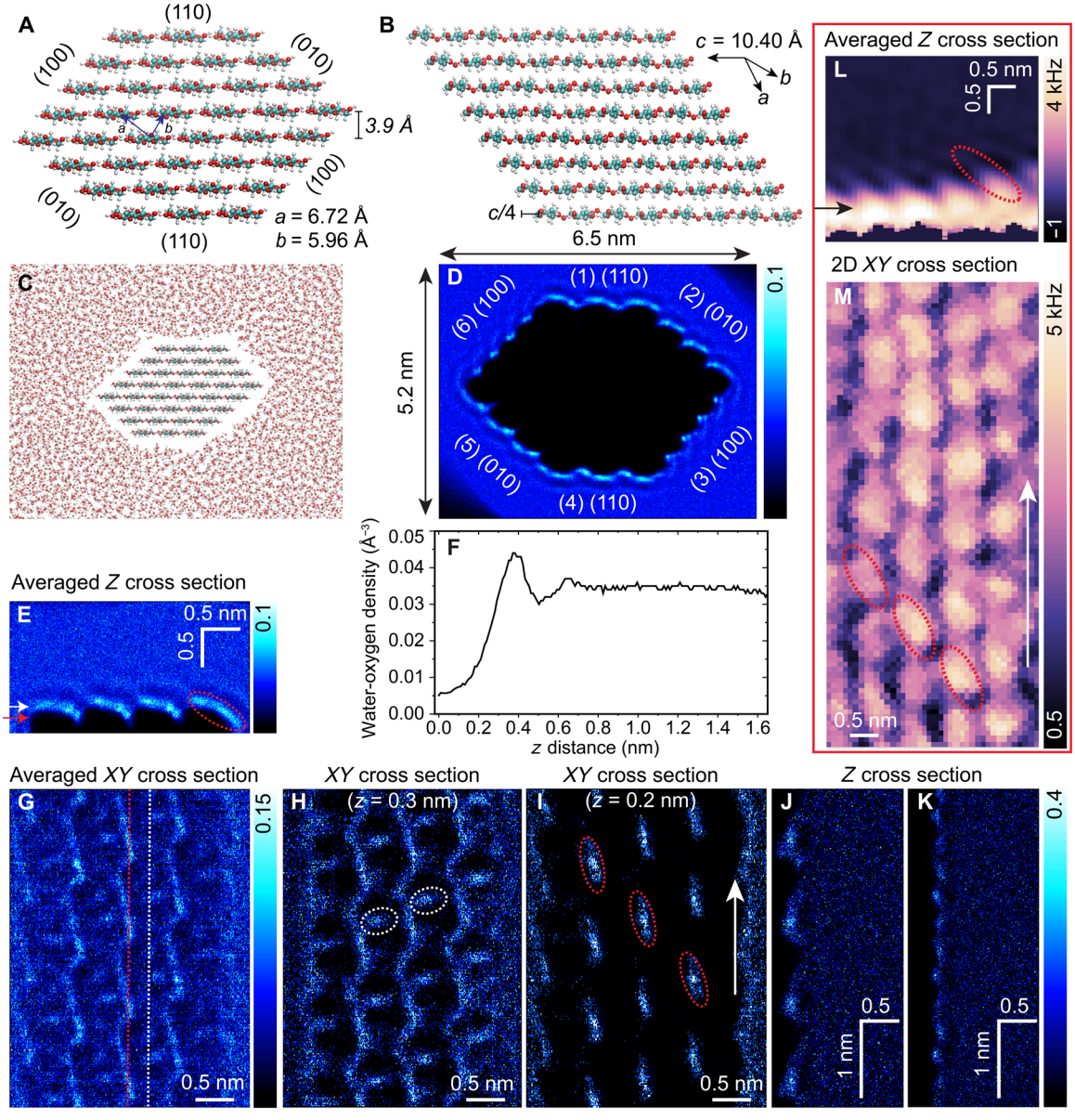

Fig. 5. Simulated water-density distribution around different crystalline planes of a CNC surface. (**A**) A 36-chain microfibril model of cellulose I_α crystalline structure with a hexagonal shape generated with Cellulose Builder software, displaying different crystallographic planes. (**B**) A longitudinal view of parallel sheets of cellulose chains. Each molecular sheet is shifted along the *c* axis by + *c*/4. (**C**) An MD snapshot of CNC in water. The *c* axis is perpendicular to the image plane. (**D**) 3D simulated water oxygen density map around a hexagonal-shaped CNC with crystalline planes labeled. (**E**) Averaged vertical 2D density map of water oxygen atoms above the (010) crystalline plane, taken through *zx* plane along the perpendicular direction to the chain axis. (**F**) Averaged 1D water density profile along the surface normal. (**G**) Averaged 2D horizontal water density map, revealing the zigzag nature of the in-plane arrangement of water molecules near the crystal surface. (**H** and **I**) 2D horizontal water density slices extracted from the 3D map at the vertical positions marked with white and red arrows in (E), respectively. (**J** and **K**) 2D vertical water density maps extracted from the 3D maps, taken along the dashed red and white lines in (G), respectively. (**L** and **M**) Experimentally obtained vertical and horizontal 2D Δf maps of the cellulose-water interface, respectively.

labeled as number 2 agree with the experimentally observed hydration structures (Figs. 3 and 4). In particular, the observed zigzag or honeycomb-like molecular patterns were well reproduced by the simulated 2D in-plane density distributions of the water oxygen atoms at the (010) crystalline interface (Fig. 5, G and H), where the highly confined water molecules were organized into a zigzag pattern aligned along the cellulose molecular axis. The hydration features appearing between the zigzag patterns (marked with dashed white ellipses in Fig. 3, B and E) are also consistent with the MD simulations (Fig. 5H). Figure 5 (H and I) demonstrates the evolution of the 2D in-plane molecular organizations of water oxygens through the hydration layers when moving from a vertical distance of $z = 0.3$ to $z = 0.2$ nm (Fig. 5, H and I). In line with the 3D-AFM measurements, we found that the zigzag water density pattern changed to diagonally aligned, extended protruding features that appeared at a vertical distance relatively closer to the cellulose surface (Fig. 5I). This molecular

arrangement of water is consistent with the observed bright protruding molecular features, as shown in the 2D planar Δf maps in Figs. 4 (D and E) and 5M. The appearance of honeycomb or zigzag arrangements of hydration structures relatively far from the cellulose surface is evident from the horizontal 2D Δf maps in Figs. 3 (B and E) and 4F, which agrees with the 2D density distribution data shown in Fig. 5 (G and H).

To gain further insight into the interfacial water structuring, we examined in detail the vertical organization of water molecules above the crystalline plane labeled with number 2. Figure 5E shows the averaged calculated vertical 2D density map of water oxygen atoms reconstructed from the 3D density map along the direction perpendicular to the cellulose molecular axis. The resulting vertical water density profile closely followed the rugged contours of the surface molecular corrugations (fig. S8, E and F), resulting in pronounced patterning of water molecules that exhibit an undulating appearance, similar to the experimentally observed 2D vertical Δf map (Fig. 5L and fig. S5F). Notably, although the vertical water density profile determined over the crystalline plane labeled with number 1 yielded very similar water structuring to that of the crystalline plane 2 (Fig. 5, J and K, and fig. S10, F and G), substantial differences were observed in the spatial distribution of water molecules in the lateral *xy* plane (fig. S10). A detailed comparison of the simulated 2D horizontal and vertical water oxygen density distributions above the other crystalline planes is provided in figs. S9 and S10.

To better understand the water structuring above the CNC surface, we performed an HB analysis. We determined the average number of HBs formed between the water molecules at the interface and the possible sites on the crystalline cellulose surface (Fig. 6A). The most significant HBs were detected between the water molecules and the cellulose hydroxyl groups present in the hydroxymethyl groups (labeled O11 in Fig. 6B). Thus, the in-plane organization of water molecules and their extension from the substrate are mainly determined by the specific surface arrangement of OH groups and their accessibility for hydrogen-bonding interactions with water molecules. The crystalline planes with higher molecular corrugation and wider grooves have stronger interactions with the surrounding water molecules (*51*), thus allowing better water structuring due to increased hydrogen bonding capability. As can be inferred from a comparison of the molecular structure of the underlying crystalline plane with the water density distribution (fig. S8, D to F), the water molecules approach the crystal surface either above the surface sites between the cellulose chains or through the surface grooves and can engage in the formation of HBs with the exposed surface OH groups present in the cellulose chains.

On the basis of the density distribution data in Fig. 5 and the HBs analyzed from the MD trajectories (Fig. 6), we conclude that the regions marked with red dashed ovals in the vertical 2D Δf maps (Fig. 4, G to I) are associated with the areas where the interfacial water molecules form HBs with the OH groups on the cellulose chains, and the regions with darker contrast (highlighted with white dashed ellipses) between these regions represent the regions where no HBs are formed between the water molecules and the surface hydroxyl or other nearby functional groups.

DISCUSSION

We performed 3D-AFM experiments and MD simulations to characterize the structure of the crystalline cellulose-water interfaces. Surface structural defects associated with the amorphous regions of cellulose were identified on a single CNC fiber, which consists of crystalline domains interspersed with disordered regions distributed at irregular intervals along its length. Characterizing these nanoscale imperfections at the single-CNC fiber level is essential for developing processes for deconstructing cellulose to produce renewable nanomaterials relevant to energy, biofuels, and other biochemical products.

The 3D-AFM experiments combined with the MD simulations revealed that the interaction of water molecules with the CNC surface led to substantial structuring of the interface. The substantial differences observed in the molecular details of water structuring at different interfaces, as revealed by AFM experiments and water-oxygen density distributions determined by MD simulations, reflect the heterogeneous nature of the interactions between CNCs and water at the molecular level. The inhomogeneous existence of these structured water layers on different crystalline planes may affect the CNC surface adsorption and interaction behavior; thus,

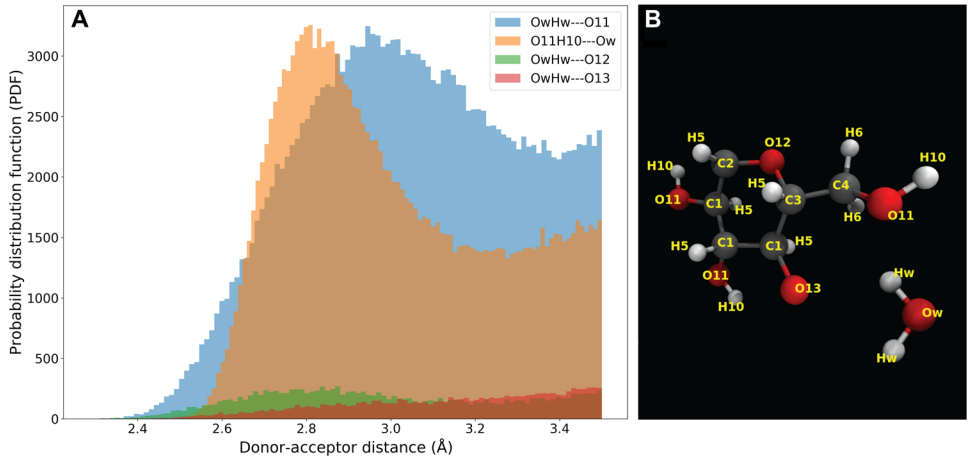

Fig. 6. HB analysis. (**A**) HB analysis between the possible cellulose sites and water molecules, showing the distribution of the number of HBs. (**B**) Atomic structures of cellulose chain and water with the respective atomic labels used in the HB analysis. Cellulose and water molecules are displayed in a ball-and-stick model. Many HBs were detected between water molecules and cellulose hydroxyl groups located in hydroxymethyl groups.

the degradation of cellulose by cellulose-degrading enzymes could be affected differently. The facet-dependent hydration structures at the interface might also affect the reactivity of the CNC surface against molecular adsorption, diffusion, and chemical reactions. On the basis of the results of the MD simulations, it has been hypothesized (*21*) that these hydration layers might act as kinetic barriers and preclude the approach of enzymes/proteins and other biomolecules to cellulose surfaces. They may also block the escape routes of the hydrolysis products from the interface and contribute to the slowing of the reaction rate in cellulose conversion processes over time (*42*). The 3D spatial organization of water molecules at the interface is thus an essential factor for understanding and modeling hydrolysis kinetics.

On the other hand, the formation of percolating CNC networks has been reported to improve the mechanical properties of composite nanomaterials (*19*). These rigid percolated networks formed between CNCs exhibit stimuli-responsive mechanical properties (*19*, *65*). Anisotropic water structuring at different crystalline interfaces can modulate the percolated networks among CNCs and promote stimuli-responsive behavior in hybrid systems involving CNCs.

Characterization of CNC surfaces with molecular-scale spatial resolution is crucial for understanding their structural properties. This is also important for the control and design of new cellulose-based functional materials (*66*). Furthermore, detailed characterization of the 3D local hydration structures and their spatial distribution around the different surfaces of CNCs with molecular resolution would contribute to a better understanding of the degradation processes (*26*). Overall, our findings will contribute toward elucidating the structure-property relationships occurring at the surfaces of CNCs and enhance our understanding of their recalcitrance to enzymatic and chemical hydrolysis. The present study represents an essential step toward understanding the mechanisms of CNC degradation, which is crucial for biomass conversion, with relevance to renewable nanomaterials and chemical production. Moreover, this work demonstrates the capabilities of 3D AFM to provide molecular resolution of complex biomaterial interfaces with water, where small-amplitude measurements allow for detailed characterization of the hydration structures around even 3D nanostructures (*67*, *68*).

MATERIALS AND METHODS

Preparation of CNCs

The CNCs used here were prepared by sulfuric acid hydrolysis of native cellulose from coconut gels, following the procedure described in (*69*). The use of sulfuric acid in the hydrolysis process can esterify the hydroxyl (OH) groups of cellulose with sulfate groups, introducing negatively charged sulfate ester ($-OSO_3^-$) groups onto the CNC surfaces, which can improve the colloidal stability of CNCs due to electrostatic double-layer repulsion. Partial substitution of OSO_3^- groups occurred over the C6-OH groups exposed on crystalline cellulose surfaces (Fig. 1A). To prepare aqueous suspensions of CNCs, an aqueous suspension of CNCs [3.35 weight % (wt%)] was first diluted to a concentration of 0.008 wt% in Milli-Q water. The suspension was then sonicated using an ultrasonic homogenizer (Mitsui, 3-mm diameter tip, maximum power of 500 W) to disintegrate the cellulose fragments. The samples were placed in an ice bath to prevent excessive heating during the sonication process and were sonicated thrice for 3 min. The CNCs used in AFM studies were prepared by placing a few drops of dilute CNC suspension (100 μl) onto a freshly cleaved mica substrate previously exposed to APTES vapors (to reverse the surface charge of mica) for 15 min in a vacuum desiccator. After the 15-min incubation of the CNC suspension, the substrate was rinsed several times with Milli-Q water to further lower the concentration of CNCs and remove the unbound CNC entities. A brief sonication process was performed before the CNC suspension was placed on a freshly prepared APTES-modified mica substrate to prevent the formation of CNC aggregates. We also used poly-L-lysine–coated mica for AFM observations.

A glass container containing 30 μl of APTES solution was placed at the bottom of the desiccator, and a freshly cleaved mica substrate was mounted on a plastic tray 5 cm above. Silanization was performed under an APTES atmosphere for approximately 25 min. The APTES-modified sample was stored in a desiccator overnight and later used for AFM observations.

Frequency modulation AFM experiments

The experiments were carried out with a custom-built frequency modulation AFM system operating in liquid environments and equipped with an ultralow-noise cantilever deflection sensor (*70*). The oscillation of the cantilever was driven by photothermal excitation. The AFM scanning process was controlled using a commercial SPM controller (ARC2, Asylum Research). A constant cantilever oscillation amplitude was maintained by adjusting the excitation signal amplitude using a commercially available controller (OC4, SPECS). The AFM was operated in the constant frequency shift (Δf) mode, where the tip-sample distance was adjusted such that Δf was kept constant. AFM image data were acquired using a commercially available silicon cantilever (160 AC-NG, OPUS) with a nominal spring constant of 25 N/m. The nominal apex radius of the Si tip was ~7 nm. The cantilever spring constants were calibrated using the thermal noise method after each experiment. AFM image processing and analysis were performed using WSxM image analysis software (*71*). The raw AFM data were postprocessed by flattening and plane-fitting to eliminate background tilt where necessary. The scanning parameters, including the scan angle, imaging set point, and rate, were varied to obtain the optimum contrast of the surface features in the AFM images. We realized that the interface structural features were best resolved when the CNC molecular axis was oriented parallel to the probe fast-scan direction or at an angle of 45°.

Following the procedures described in (*72*), we performed 3D-AFM force mapping experiments to characterize the 3D hydration structures near the CNC surface. The 3D Δf maps of the cellulose-water interfaces were obtained using a homemade 3D-AFM system (*73*), where a fast sinusoidal signal was additionally applied to the *z*-piezo to control the tip's *z* position during image acquisition and force mapping. The applied *z*-piezo signal was synchronized with the lateral *xy* scans of the tip, where Δf was recorded for each tip position, while the average tip-sample distance was regulated so that the average value of the Δf set point was kept constant. A 3D-Δf map covering an area of (5 to 12) nm by (5 to 12) nm was acquired by real-time recording of Δf with respect to the tip positions in the 3D interfacial space at the interface between the cellulose NC and water. The typical resolution of the 3D Δf datasets was 128 × 128 pixels laterally and 256 pixels vertically, before data processing. The cantilever oscillation amplitudes were set in the range of 0.1 to 0.25 nm (smaller than the size of a water molecule) to resolve the distribution of local hydration layers.

The maxima in the Δf shifts were interpreted as the maxima in the water density distribution based on the solvent tip approximation (STA) (*74*). Thus, the observed features in the solvation layers found

in the 2D/3D Δf maps are related to changes in water density. The force map derived from the STA model showed hydration features that were almost identical to those of the water density maps (fig. S11). A comparison of the vertical 2D Δf map and the 2D force map is shown in fig. S12. The similarity of the force and Δf map is evident, thus validating that the water oxygen density maps can, in principle, be directly compared with the Δf maps for interpreting the observed hydration structures near the CNC surfaces (see Supplementary Text for further discussion). The validity of this approach has been demonstrated for different solid-liquid interfaces (*57*, *58*, *74*). For the particular case of heterogeneous surfaces, earlier studies on these systems demonstrated that the AFM contrast remains dominated by the first hydration layer (*75*).

Computational details

The cellulose structure and topology were obtained using the "Cellulose–builder" computational toolkit developed in (*76*), which uses the CHARMM36 force field. Following the model proposed by Ding and Himmel (*64*), a 36-chain, hexagonal-shaped cellulose-I_α nanocrystal was assembled and repeated three times along the z direction. Periodic boundary conditions were imposed along the z direction to make the crystal infinitely long. The I_α structure was obtained from the x-ray crystallographic data determined by Nishiyama *et al.* (*77*). The CNC structure was solvated using Packmol (*78*) in a simulation box with dimensions of 26.65 nm by 26.42 nm by 3.15 nm, periodically repeating in all directions to simulate an infinite CNC. The system consisted of 30,048 atoms in total (6048 atoms for cellulose and 24,000 for water). The MD simulations were carried out using the LAMMPS package (*79*), and the input files for LAMMPS were prepared using Moltemplate (*80*). We used the CHARMM36 force field with the TIP3P water model to describe the cellulose interatomic interactions and capture cellulose-water interactions. The system was equilibrated for 4 ns, using an integration time step of 1 fs. The production run was carried out in the isochoric-isothermal (NVT) ensemble for 10 ns using a Nosé-Hoover thermostat with T = 300 K and a damping parameter τ = 0.1 ps. Lennard-Jones interactions were computed with a 9-Å cutoff, whereas for the electrostatic interactions, the particle-particle-particle mesh solver (*81*) was used using a 12-Å cutoff for real-space electrostatics, with an accuracy of 10^{-6}. HB analyses were performed using the MDAnalysis software (*82*). The criteria used for identifying HBs were a maximum distance of 0.35 nm between water-oxygen and cellulose-oxygens and a donor-hydrogen-acceptor angle of 100°. Last, water-oxygen densities were extracted using MDAnalysis, using a 0.1-Å grid spacing and a total of 1000 frames, each sampled every 10 ps during the production run. Water density was computed for the MD trajectory and then averaged for each crystal plane in the lateral and vertical directions.

SUPPLEMENTARY MATERIALS

Supplementary material for this article is available at https://science.org/doi/10.1126/sciadv.abq0160

REFERENCES AND NOTES

1. R. J. Moon, A. Martini, J. Nairn, J. Simonsen, J. Youngblood, Cellulose nanomaterials review: Structure, properties and nanocomposites. *Chem. Soc. Rev.* **40**, 3941 (2011).
2. J. A. Kelly, A. M. Shukaliak, C. C. Y. Cheung, K. E. Shopsowitz, W. Y. Hamad, M. J. MacLachlan, Responsive photonic hydrogels based on nanocrystalline cellulose. *Angew. Chem. Int. Ed.* **52**, 8912–8916 (2013).
3. M. Giese, L. K. Blusch, M. K. Khan, M. J. MacLachlan, Functional materials from cellulose-derived liquid-crystal templates. *Angew. Chem. Int. Ed.* **54**, 2888–2910 (2015).
4. Y. H. Jung, T.-H. Chang, H. Zhang, C. Yao, Q. Zheng, V. W. Yang, H. Mi, M. Kim, S. J. Cho, D.-W. Park, H. Jiang, J. Lee, Y. Qiu, W. Zhou, Z. Cai, S. Gong, Z. Ma, High-performance green flexible electronics based on biodegradable cellulose nanofibril paper. *Nat. Commun.* **6**, 7170 (2015).
5. F. J. Martin-Martinez, K. Jin, D. López Barreiro, M. J. Buehler, The rise of hierarchical nanostructured materials from renewable sources: Learning from nature. *ACS Nano* **12**, 7425–7433 (2018).
6. B. G. Rånby, E. Ribi, Über den Feinbau der Zellulose. *Experientia* **6**, 12–14 (1950).
7. B. G. Rånby, Fibrous macromolecular systems. Cellulose and muscle. The colloidal properties of cellulose micelles. *Discuss. Faraday Soc.* **11**, 158–164 (1951).
8. Y. Habibi, L. A. Lucia, O. J. Rojas, Cellulose nanocrystals: Chemistry, self-assembly, and applications. *Chem. Rev.* **110**, 3479–3500 (2010).
9. J.-F. Revol, H. Bradford, J. Giasson, R. H. Marchessault, D. G. Gray, Helicoidal self-ordering of cellulose microfibrils in aqueous suspension. *Int. J. Biol. Macromol.* **14**, 170–172 (1992).
10. O. M. Vanderfleet, E. D. Cranston, Production routes to tailor the performance of cellulose nanocrystals. *Nat. Rev. Mater.* **6**, 124–144 (2021).
11. C. Liu, H. Du, L. Dong, X. Wang, Y. Zhang, G. Yu, B. Li, X. Mu, H. Peng, H. Liu, Properties of nanocelluloses and their application as rheology modifier in paper coating. *Ind. Eng. Chem. Res.* **56**, 8264–8273 (2017).
12. D. Trache, M. H. Hussin, M. K. M. Haafiz, V. K. Thakur, Recent progress in cellulose nanocrystals: Sources and production. *Nanoscale* **9**, 1763–1786 (2017).
13. S. Salimi, R. Sotudeh-Gharebagh, R. Zarghami, S. Y. Chan, K. H. Yuen, Production of nanocellulose and its applications in drug delivery: A critical review. *ACS Sustain. Chem. Eng.* **7**, 15800–15827 (2019).
14. S. Ustunel, M. E. Prévôt, G. A. R. Rohaley, C. R. Webb, B. Yavitt, G. Freychet, M. Zhernenkov, R. Pindak, E. Schaible, C. Zhu, T. Hegmann, R. J. Clements, E. Hegmann, Mechanically tunable elastomer and cellulose nanocrystal composites as scaffolds for in vitro cell studies. *Mater. Adv.* **2**, 464–476 (2021).
15. D. Zhao, Y. Zhu, W. Cheng, W. Chen, Y. Wu, H. Yu, Cellulose-based flexible functional materials for emerging intelligent electronics. *Adv. Mater.* **33**, 2000619 (2021).
16. R. M. A. Domingues, M. E. Gomes, R. L. Reis, The potential of cellulose nanocrystals in tissue engineering strategies. *Biomacromolecules* **15**, 2327–2346 (2014).
17. A. Espinha, C. Dore, C. Matricardi, M. I. Alonso, A. R. Goñi, A. Mihi, Hydroxypropyl cellulose photonic architectures by soft nanoimprinting lithography. *Nat. Photonics* **12**, 343–348 (2018).
18. C. E. Boott, M. A. Soto, W. Y. Hamad, M. J. MacLachlan, Shape-memory photonic thermoplastics from cellulose nanocrystals. *Adv. Funct. Mater.* **31**, 2103268 (2021).
19. R. Sinko, S. Keten, Effect of moisture on the traction-separation behavior of cellulose nanocrystal interfaces. *Appl. Phys. Lett.* **105**, 243702 (2014).
20. R. Sinko, X. Qin, S. Keten, Interfacial mechanics of cellulose nanocrystals. *MRS Bulletin* **40**, 340–348 (2015).
21. J. F. Matthews, C. E. Skopec, P. E. Mason, P. Zuccato, R. W. Torget, J. Sugiyama, M. E. Himmel, J. W. Brady, Computer simulation studies of microcrystalline cellulose I_β. *Carbohydr. Res.* **341**, 138–152 (2006).
22. E. Malm, V. Bulone, K. Wickholm, P. T. Larsson, T. Iversen, The surface structure of well-ordered native cellulose fibrils in contact with water. *Carbohydr. Res.* **345**, 97–100 (2010).
23. A. P. Heiner, L. Kuutti, O. Teleman, Comparison of the interface between water and four surfaces of native crystalline cellulose by molecular dynamics simulations. *Carbohydr. Res.* **306**, 205–220 (1998).
24. A. P. Heiner, O. Teleman, Interface between monoclinic crystalline cellulose and water: Breakdown of the odd/even duplicity. *Langmuir* **13**, 511–518 (1997).
25. A. J. Ragauskas, C. K. Williams, B. H. Davison, G. Britovsek, J. Cairney, C. A. Eckert, W. J. Frederick, J. P. Hallett, D. J. Leak, C. L. Liotta, J. R. Mielenz, R. Murphy, R. Templer, T. Tschaplinski, The path forward for biofuels and biomaterials. *Science* **311**, 484–489 (2006).
26. L. Petridis, J. C. Smith, Molecular-level driving forces in lignocellulosic biomass deconstruction for bioenergy. *Nat. Rev. Chem.* **2**, 382–389 (2018).
27. A. Tran, C. E. Boott, M. J. MacLachlan, Understanding the self-assembly of cellulose nanocrystals—Toward chiral photonic materials. *Adv. Mater.* **32**, 1905876 (2020).
28. I. Usov, G. Nyström, J. Adamcik, S. Handschin, C. Schütz, A. Fall, L. Bergström, R. Mezzenga, Understanding nanocellulose chirality and structure–properties relationship at the single fibril level. *Nat. Commun.* **6**, 7564 (2015).
29. K. L. Stinson-Bagby, R. Roberts, E. J. Foster, Effective cellulose nanocrystal imaging using transmission electron microscopy. *Carbohydr. Polym.* **186**, 429–438 (2018).
30. W. Helbert, Y. Nishiyama, T. Okano, J. Sugiyama, Molecular imaging of Halocynthia papillosa cellulose. *J. Struct. Biol.* **124**, 42–50 (1998).
31. J. Sugiyama, H. Harada, Y. Fujiyoshi, N. Uyeda, Lattice images from ultrathin sections of cellulose microfibrils in the cell wall of Valonia macrophysa Kütz. *Planta* **166**, 161–168 (1985).

32. J.-F. Revol, On the cross-sectional shape of cellulose crystallites in *Valonia ventricosa*. *Carbohydr. Polym.* **2**, 123–134 (1982).
33. S. Elazzouzi-Hafraoui, Y. Nishiyama, J.-L. Putaux, L. Heux, F. Dubreuil, C. Rochas, The shape and size distribution of crystalline nanoparticles prepared by acid hydrolysis of native cellulose. *Biomacromolecules* **9**, 57–65 (2008).
34. R. R. Lahiji, X. Xu, R. Reifenberger, A. Raman, A. Rudie, R. J. Moon, Atomic force microscopy characterization of cellulose nanocrystals. *Langmuir* **26**, 4480–4488 (2010).
35. S. Iwamoto, W. Kai, A. Isogai, T. Iwata, Elastic modulus of single cellulose microfibrils from tunicate measured by atomic force microscopy. *Biomacromolecules* **10**, 2571–2576 (2009).
36. S. J. Hanley, J.-F. Revol, L. Godbout, D. G. Gray, Atomic force microscopy and transmission electron microscopy of cellulose from Micrasterias denticulata; evidence for a chiral helical microfibril twist. *Cellulose* **4**, 209–220 (1997).
37. K. Igarashi, T. Uchihashi, A. Koivula, M. Wada, S. Kimura, T. Okamoto, M. Penttilä, T. Ando, M. Samejima, Traffic jams reduce hydrolytic efficiency of cellulase on cellulose surface. *Science* **333**, 1279–1282 (2011).
38. M. Eibinger, J. Sattelkow, T. Ganner, H. Plank, B. Nidetzky, Single-molecule study of oxidative enzymatic deconstruction of cellulose. *Nat. Commun.* **8**, 894 (2017).
39. A. A. Baker, W. Helbert, J. Sugiyama, M. J. Miles, High-resolution atomic force microscopy of native valonia cellulose I microcrystals. *J. Struct. Biol.* **119**, 129–138 (1997).
40. A. A. Baker, W. Helbert, J. Sugiyama, M. J. Miles, Surface structure of native cellulose microcrystals by AFM. *Appl. Phys. A* **66**, S559–S563 (1998).
41. A. A. Baker, W. Helbert, J. Sugiyama, M. J. Miles, New insight into cellulose structure by atomic force microscopy shows the I_α crystal phase at near-atomic resolution. *Biophys. J.* **79**, 1139–1145 (2000).
42. J. R. K. Nutor, A. O. Converse, The effect of enzyme and substrate levels on the specific hydrolysis rate of pretreated poplar wood. *Appl. Biochem. Biotechnol.* **28-29**, 757–772 (1991).
43. E. J. Foster, R. J. Moon, U. P. Agarwal, M. J. Bortner, J. Bras, S. Camarero-Espinosa, K. J. Chan, M. J. D. Clift, E. D. Cranston, S. J. Eichhorn, D. M. Fox, W. Y. Hamad, L. Heux, B. Jean, M. Korey, W. Nieh, K. J. Ong, M. S. Reid, S. Renneckar, R. Roberts, J. A. Shatkin, J. Simonsen, K. Stinson-Bagby, N. Wanasekara, J. Youngblood, Current characterization methods for cellulose nanomaterials. *Chem. Soc. Rev.* **47**, 2609–2679 (2018).
44. I. A. Sacui, R. C. Nieuwendaal, D. J. Burnett, S. J. Stranick, M. Jorfi, C. Weder, E. J. Foster, R. T. Olsson, J. W. Gilman, Comparison of the properties of cellulose nanocrystals and cellulose nanofibrils isolated from bacteria, tunicate, and wood processed using acid, enzymatic, mechanical, and oxidative methods. *ACS Appl. Mater. Interfaces* **6**, 6127–6138 (2014).
45. S. J. Hanley, J. Giasson, J.-F. Revol, D. G. Gray, Atomic force microscopy of cellulose microfibrils: Comparison with transmission electron microscopy. *Polymer* **33**, 4639–4642 (1992).
46. F. Cherhal, F. Cousin, I. Capron, Influence of charge density and ionic strength on the aggregation process of cellulose nanocrystals in aqueous suspension, as revealed by small-angle neutron scattering. *Langmuir* **31**, 5596–5602 (2015).
47. T. Fukuma, B. Reischl, N. Kobayashi, P. Spijker, F. F. Canova, K. Miyazawa, A. S. Foster, Mechanism of atomic force microscopy imaging of three-dimensional hydration structures at a solid-liquid interface. *Phys. Rev. B* **92**, 155412 (2015).
48. T. Arioli, L. Peng, A. S. Betzner, J. Burn, W. Wittke, W. Herth, C. Camilleri, H. Höfte, J. Plazinski, R. Birch, A. Cork, J. Glover, J. Redmond, R. E. Williamson, Molecular analysis of cellulose biosynthesis in Arabidopsis. *Science* **279**, 717–720 (1998).
49. T. Wang, M. Hong, Solid-state NMR investigations of cellulose structure and interactions with matrix polysaccharides in plant primary cell walls. *J. Exp. Bot.* **67**, 503–514 (2016).
50. A. Paajanen, S. Ceccherini, T. Maloney, J. A. Ketoja, Chirality and bound water in the hierarchical cellulose structure. *Cellulose* **26**, 5877–5892 (2019).
51. Z. Ren, R. Guo, H. Bi, X. Jia, M. Xu, L. Cai, Interfacial adhesion of polylactic acid on cellulose surface: A molecular dynamics study. *ACS Appl. Mater. Interfaces* **12**, 3236–3244 (2020).
52. K. Wickholm, P. T. Larsson, T. Iversen, Assignment of non-crystalline forms in cellulose I by CP/MAS ^{13}C NMR spectroscopy. *Carbohydr. Res.* **312**, 123–129 (1998).
53. R. H. Atalla, D. L. VanderHart, Native cellulose: A composite of two distinct crystalline forms. *Science* **223**, 283–285 (1984).
54. M. Koyama, W. Helbert, T. Imai, J. Sugiyama, B. Henrissat, Parallel-up structure evidences the molecular directionality during biosynthesis of bacterial cellulose. *Proc. Natl. Acad. Sci. U.S.A.* **94**, 9091–9095 (1997).
55. P. T. Larsson, U. Westermark, T. Iversen, Determination of the cellulose I_α allomorph content in a tunicate cellulose by CP/MAS ^{13}C-NMR spectroscopy. *Carbohydr. Res.* **278**, 339–343 (1995).
56. Y. Nishiyama, P. Langan, H. Chanzy, Crystal structure and hydrogen-bonding system in cellulose I_β from synchrotron x-ray and neutron fiber diffraction. *J. Am. Chem. Soc.* **124**, 9074–9082 (2002).
57. K. Umeda, L. Zivanovic, K. Kobayashi, J. Ritala, H. Kominami, P. Spijker, A. S. Foster, H. Yamada, Atomic-resolution three-dimensional hydration structures on a heterogeneously charged surface. *Nat. Commun.* **8**, 2111 (2017).
58. K. Miyata, J. Tracey, K. Miyazawa, V. Haapasilta, P. Spijker, Y. Kawagoe, A. S. Foster, K. Tsukamoto, T. Fukuma, Dissolution processes at step edges of calcite in water investigated by high-speed frequency modulation atomic force microscopy and simulation. *Nano Lett.* **17**, 4083–4089 (2017).
59. H. Söngen, B. Reischl, K. Miyata, R. Bechstein, P. Raiteri, A. L. Rohl, J. D. Gale, T. Fukuma, A. Kühnle, Resolving point defects in the hydration structure of calcite (10.4) with three-dimensional atomic force microscopy. *Phys. Rev. Lett.* **120**, 116101 (2018).
60. K. Kuchuk, U. Sivan, Hydration structure of a single DNA molecule revealed by frequency-modulation atomic force microscopy. *Nano Lett.* **18**, 2733–2737 (2018).
61. M. R. Uhlig, D. Martin-Jimenez, R. Garcia, Atomic-scale mapping of hydrophobic layers on graphene and few-layer MoS_2 and WSe_2 in water. *Nat. Commun.* **10**, 2606 (2019).
62. E. Nakouzi, A. G. Stack, S. Kerisit, B. A. Legg, C. J. Mundy, G. K. Schenter, J. Chun, J. J. De Yoreo, Moving beyond the solvent-tip approximation to determine site-specific variations of interfacial water structure through 3D force microscopy. *J. Phys. Chem. C* **125**, 1282–1291 (2021).
63. A. N. Fernandes, L. H. Thomas, C. M. Altaner, P. Callow, V. T. Forsyth, D. C. Apperley, C. J. Kennedy, M. C. Jarvis, Nanostructure of cellulose microfibrils in spruce wood. *Proc. Natl. Acad. Sci. U.S.A.* **108**, E1195–E1203 (2011).
64. S.-Y. Ding, M. E. Himmel, The maize primary cell wall microfibril: A new model derived from direct visualization. *J. Agric. Food Chem.* **54**, 597–606 (2006).
65. J. R. Capadona, K. Shanmuganathan, D. J. Tyler, S. J. Rowan, C. Weder, Stimuli-responsive polymer nanocomposites inspired by the sea cucumber dermis. *Science* **319**, 1370–1374 (2008).
66. M. E. Lamm, K. Li, J. Qian, L. Wang, N. Lavoine, R. Newman, D. J. Gardner, T. Li, L. Hu, A. J. Ragauskas, H. Tekinalp, V. Kunc, S. Ozcan, Recent advances in functional materials through cellulose nanofiber templating. *Adv. Mater.* **33**, 2005538 (2021).
67. F. J. Giessibl, Advances in atomic force microscopy. *Rev. Mod. Phys.* **75**, 949–983 (2003).
68. S. Jeffery, P. M. Hoffmann, J. B. Pethica, C. Ramanujan, H. Ö. Özer, A. Oral, Direct measurement of molecular stiffness and damping in confined water layers. *Phys. Rev. B* **70**, 054114 (2004).
69. S. Beck-Candanedo, M. Roman, D. G. Gray, Effect of reaction conditions on the properties and behavior of wood cellulose nanocrystal suspensions. *Biomacromolecules* **6**, 1048–1054 (2005).
70. T. Fukuma, Wideband low-noise optical beam deflection sensor with photothermal excitation for liquid-environment atomic force microscopy. *Rev. Sci. Instrum.* **80**, 023707 (2009).
71. I. Horcas, R. Fernández, J. M. Gómez-Rodríguez, J. Colchero, J. Gómez-Herrero, A. M. Baro, WSXM: A software for scanning probe microscopy and a tool for nanotechnology. *Rev. Sci. Instrum.* **78**, 013705 (2007).
72. A. Yurtsever, P. X. Wang, F. Priante, Y. Morais Jaques, K. Miyata, M. J. MacLachlan, A. S. Foster, T. Fukuma, Probing the structural details of chitin nanocrystal–water interfaces by three-dimensional atomic force microscopy. *Small Methods* **6**, 2200320 (2022).
73. T. Fukuma, Y. Ueda, S. Yoshioka, H. Asakawa, Atomic-scale distribution of water molecules at the mica-water interface visualized by three-dimensional scanning force microscopy. *Phys. Rev. Lett.* **104**, 016101 (2010).
74. M. Watkins, B. Reischl, A simple approximation for forces exerted on an AFM tip in liquid. *J. Chem. Phys.* **138**, 154703 (2013).
75. P. Spijker, T. Hiasa, T. Musso, R. Nishioka, H. Onishi, A. S. Foster, Understanding the interface of liquids with an organic crystal surface from atomistic simulations and AFM experiments. *J. Phys. Chem. C* **118**, 2058–2066 (2014).
76. T. C. F. Gomes, M. S. Skaf, Cellulose-Builder: A toolkit for building crystalline structures of cellulose. *J. Comput. Chem.* **33**, 1338–1346 (2012).
77. Y. Nishiyama, J. Sugiyama, H. Chanzy, P. Langan, Crystal structure and hydrogen bonding system in cellulose i_α from synchrotron x-ray and neutron fiber diffraction. *J. Am. Chem. Soc.* **125**, 14300–14306 (2003).
78. L. Martínez, R. Andrade, E. G. Birgin, J. M. Martínez, PACKMOL: A package for building initial configurations for molecular dynamics simulations. *J. Comput. Chem.* **30**, 2157–2164 (2009).
79. S. Plimpton, Fast parallel algorithms for short-range molecular dynamics. *J. Comput. Phys.* **117**, 1–19 (1995).
80. A. I. Jewett, D. Stelter, J. Lambert, S. M. Saladi, O. M. Roscioni, M. Ricci, L. Autin, M. Maritan, S. M. Bashusqeh, T. Keyes, R. T. Dame, J. E. Shea, G. J. Jensen, D. S. Goodsell, Moltemplate: A tool for coarse-grained modeling of complex biological matter and soft condensed matter physics. *J. Mol. Biol.* **433**, 166841 (2021).
81. R. W. Hockney, J. W. Eastwood, *Computer Simulation Using Particles* (McGraw-Hill, 1981).
82. N. Michaud-Agrawal, E. J. Denning, T. B. Woolf, O. Beckstein, MDAnalysis: A toolkit for the analysis of molecular dynamics simulations. *J. Comput. Chem.* **32**, 2319–2327 (2011).

Acknowledgments: We thank the World Premier International Research Center Initiative (WPI), the Ministry of Education, Culture, Sports, Science, and Technology (MEXT), Japan, and Kanazawa University Fund (Strategic Research Promotion Program, Core-to-Core Program).

The computing resources from the Aalto Science-IT project, CSC, and Helsinki are gratefully acknowledged. **Funding:** We gratefully acknowledge the financial support from Grants-in-Aid for Scientific Research (nos. 21H05251, 20H00345, 19 K22125, and 20 K05321) from MEXT, Japan. The authors also acknowledge the financial support from the Natural Sciences and Engineering Research Council (NSERC Canada) (Discovery Grant F16-05032). This work was part of the Academy of Finland's Flagship Programme under project nos. 318890 and 318891 (Competence Center for Materials Bioeconomy, FinnCERES) and project no. 314862. **Author contributions:** A.Y., T.F., M.J.M., and A.S.F. conceptualized the study and designed the experiments and simulations. A.Y. performed the 3D-AFM measurements and analyzed the data. P.-X.W. and M.J.M. prepared the cellulose nanocrystals. K.M. helped with data analysis. F.P. and Y.M.J. performed the MD simulations. A.S.F. supervised the MD simulations. A.Y. wrote the manuscript with input from all authors. All authors discussed the results and contributed to the final manuscript. **Competing interests:** The authors declare that they have no competing interests. **Data and materials availability:** All data needed to evaluate the conclusions in the paper are present in the paper and/or the Supplementary Materials.

Submitted 12 March 2022
Accepted 26 August 2022
Published 14 October 2022
10.1126/sciadv.abq0160

ScienceAdvances

Molecular insights on the crystalline cellulose-water interfaces via three-dimensional atomic force microscopy

Ayhan YurtseverPei-Xi WangFabio PrianteYgor Morais JaquesKeisuke MiyazawaMark J. MacLachlanAdam S. FosterTakeshi Fukuma

Sci. Adv., 8 (41), eabq0160. • DOI: 10.1126/sciadv.abq0160

Science Advances (ISSN) is published by the American Association for the Advancement of Science. 1200 New York Avenue NW, Washington, DC 20005. The title *Science Advances* is a registered trademark of AAAS.